# Dynamic contact strain measurement by time-resolved stroboscopic energy dispersive synchrotron X-ray diffraction

M. Mostafavi[1,*], D. M. Collins[2], M. J. Peel[1], C. Reinhard[3], S. M. Barhli[2], R. Mills[4], M. B. Marshall[4], R. S. Dwyer-Joyce[4], T. Connolley[3]

[1] Department of Mechanical Engineering, University of Bristol, Bristol, UK

[2] Department of Materials, University of Oxford, Oxford, UK

[3] Joint Engineering, Environment, and Processing Beamline, Diamond Light Source, Harwell Science and Innovation Campus, Didcot, UK

[4] Department of Mechanical Engineering, University of Sheffield, Sheffield, UK

## Abstract

Recent developments of synchrotron X-ray sources and dedicated high-energy beamlines are now enabling strain measurements from large volumes of industrially relevant metallic materials. Such capability is allowing the validation of novel and alternative non-destructive experimental methods of strain measurement or computational models of complex deformation processes. This study describes the first dynamic contact strain measurement of a ball bearing using stroboscopic Energy Dispersive X-ray Diffraction (EDXD). The experiment probed the dynamic contact strain in the outer raceway of a test bearing. The inner raceway of the bearing was attached to a shaft rotating at 150 revolutions per minute and the outer raceway, where the measurements were made, was fixed in a stationary bearing housing. A triggering system was used to synchronise the data acquisition of the EDXD detector with the bearing rotation. Specifically, diffraction data was acquired, stroboscopically, from the material volume within the raceway, in a known location, when the ball was positioned directly below it. A total of 20 seconds of accumulated diffraction signal was recorded, acquiring 2 milliseconds of data per revolution, providing diffraction patterns of sufficient quality for the dynamic contact strain to be measured. Macromechanical stress field was calculated from the micromechanical strains measured from five lattice planes. This allowed a comparison of the experimentally measured stress field and that of finite element (FE) simulations. Good agreement was observed between the FE results and experimental measurements indicating the applicability of this novel dynamic strain measurement technique for tribological systems.

**keywords: Stroboscopic measurement, energy dispersive X-ray diffraction, tribology, contact stress, finite element analysis**

---

[*] Corresponding author: Mahmoud Mostafavi, Department of Mechanical Engineering, Queen's Building, University of Bristol, University Walk, Bristol, BS8 1TR

E-mail: m.mostafavi@bristol.ac.uk

# 1 Introduction

## 1.1 Background

Knowledge of the remaining life of gearbox bearings allows an operator to suitably schedule maintenance of machinery. It is therefore desirable to equip bearings with quantitative health monitoring systems. Bearings typically fail by rolling contact fatigue, with factors such as overload in the form of plastic deformation, impact damage, or buckling acting as accelerants. Since direct measurements of torque on the rotor shafts cannot reliably be used to determine the load history in the bearings, it is difficult to determine whether events such as overload, which govern the residual life of the rolling bearing [1], have occurred. This is further complicated by the applied load not being uniformly distributed on each of the rolling elements [2]. The load applied to the whole bearing, therefore, does not represent the stress state on the individual rolling elements or raceways. Advanced techniques such as acousto-elastic measurements have been developed in recent years that aim to determine the contact stress in tribological machine elements [3, 4]. However, it is difficult to validate such complex measurement techniques because, to date, there have not been alternative independent methods of dynamic in-situ measurement. Finite element simulations may be used to validate the techniques [5], although, such models themselves need validation by independent experimental techniques. X-ray and neutron diffraction techniques are now being used as routine techniques to map static micromechanical strains by measuring the change in the lattice spacing of crystalline materials (e.g. see [6]) which can be employed to validate the acousto-elastic measurements. Application of such techniques for dynamic measurements, however, have been rare. Dynamic strain measurement by a diffraction method was the objective of this study.

To select an appropriate diffraction technique, a brief comparison of the advantages and drawbacks of each technique is given here. Neutron diffraction offers higher penetration depth than X-ray diffraction. For example, the Engin-X beamline at the ISIS neutron source, UK, can measure the strain in ferritic steels with a 50 $\mu\varepsilon$ resolution and a $2\times2\times2$ mm$^3$ gauge volume at a depth of 20mm in 3-5 minutes [7]. Such measurements are suitable for engineering components but their inherently slow acquisition time makes dynamic strain measurements difficult [8–10]. Comparatively, a synchrotron high energy monochromatic X-ray powder diffraction technique allows measurements with high spatial resolution and low acquisition times. Collection times are typically seconds or less for thin sheets of steel (of the order of a couple of millimetres), making dynamic experiments feasible. However, the penetration depth is limited and only small volumes of materials can be interrogated; for example, a ferritic steel measured by a monochromatic beam at approximately 90keV on the Joint Engineering, Environmental and Processing (JEEP) beamline at Diamond Light Source, UK, with $0.5\times0.5\times0.4$ mm$^3$ gauge in 4 seconds has an accuracy of ~150 $\mu\varepsilon$ [11]. High-energy synchrotron X-ray white beam scattering (alternatively known as Energy Dispersive X-ray Diffraction – EDXD), is a comparatively fast technique with high penetration depth. The latter benefit arises from the use of the full wavelength spectrum of photons produced by synchrotron radiation, rather than the more commonly used monochromatic powder diffraction method that only uses a very narrow band of photon wavelengths. For example, we will have shown in the present study that the average strain in a gauge volume of $0.25\times0.25\times6.7$ mm$^3$ can be measured in 120 seconds with a 60 $\mu\varepsilon$ accuracy using a

white (i.e. 53 - 150 keV photons) beam. Detailed description of the EDXD technique has been published elsewhere [12].

Although stroboscopic measurement is a routine method (e.g. see a review of stroboscopic laser interferometric measurements in reference [13]), there is a very limited body of work on stroboscopic strain measurement with diffraction methods. Of note are the work by Podolsky et al. [14] who used stroboscopic small angle X-ray scattering to measure the force applied by a sartorius muscle of a frog. Wulff and co-workers [15] touched on the feasibility of stroboscopic Laue diffraction in a review of ESRF's (European Synchrotron Radiation Facility) ID09 beam-line capabilities. Harrison et al [16] used a stroboscope laboratory diffraction technique to characterise the motion of ferroelectric domain walls. Daymond and Withers used stroboscopic neutron diffraction technique to measure micromechanical strain induced within an Aluminium-SiC metal matrix composite under cyclic loading [8]. Recently, Baimpas et al. [17] measured strain in a connecting rod in a running motorcycle engine by stroboscopic EDXD at JEEP. The same technique was used in the present study to measure contact strain in the fixed raceway of a rotating ball bearing. High energy synchrotron radiation has also been used to quantify other dynamic effects. For example Brömmelhoff and co-workers used X-ray diffraction to investigate the phase transformation in chips formed during in-situ cutting at PETRA III in DESY [18].

## 1.2 Aims and structure

Our main aims in this study were to (a) measure the static strain that a ball exerts on the outer raceway of a test ball bearing when it is stationary (b) measure the dynamic strain that the ball exerts on the outer raceway of the test bearing while the bearing was rotating at 150 revolutions per minute. The outer raceway was fixed in the bearing housing and the inner raceway was attached to a rotating shaft (c) convert the static and dynamic micromechanical strains measured by EDXD to macromechanical stress and compare them with those estimated by finite element simulations. In the subsequent sections, details of the experiments and simulations are given, followed by the results obtained and finally the discussion is presented.

## 2 Methods

### 2.1 Mechanical setup

A bearing test rig was used in this study to apply loads on the test bearing while it was stationary or rotating. The bearing test rig consists of an electric motor, rotation of which is transferred to a shaft via a belt and pulley system. The shaft is supported by two self-aligning bearings 50 mm apart with the test bearing fixed in the centre within a bearing housing. Figure 1a shows a schematic cross-section of the test bearing within the bearing housing. The bearing test rig was modified to allow for the X-ray incident and diffracted beams to pass through. An ultra-slim ball bearing (REALI-SLIM, KD047CP0) with an approximately 13 mm raceway width (inner raceway diameter of 65.024 mm and outer raceway diameter of 73.025 mm) and 33 balls was selected. The relatively thin width of this bearing allows for approximately 10% transmission of the incident polychromatic x-ray beam. This was deemed to be sufficient for suitable counting statistics and data acquisition time. The bearing test rig is equipped with a lever attached to the bearing housing that encompasses the test bearing. The bearing housing is supported by a pivot, shown schematically in Figure 1a. The lever carries a deadweight which exerts a load onto the test bearing through the bearing housing. This was deemed more suitable than the more commonly used

hydraulic system as the bearing test rig was not equipped with a load cell nor a feedback loop to maintain constant oil pressure during the experiment. Preliminary tests showed that the hydraulic system gradually lost pressure and the applied load in long duration experiments (e.g. during an estimated 8 hours X-ray acquisition time) would gradually diminish, which was deemed unacceptable. Considering the low capacity of the selected test bearing, the deadweight provided enough load to induce a reasonable load (33% of the test bearing's maximum dynamic limit load).

## 2.2   Stroboscopic triggering system

The aim of the dynamic (stroboscopic) part of the experiment was to measure the contact strain exerted on the fixed outer raceway of the test bearing by a ball as it passed over the width of the gauge volume. Therefore, in stroboscopic mode, the X-ray data acquisition had to be gated on the EDXD detector, so that the data are only collected in a time interval determined by a trigger signal from the experimental equipment. It was assumed that every time the ball comes into contact with the raceway, the same strain field is developed in the raceway for 2 milliseconds calculated from the time required for the ball to travel the width of the gauge volume at 150 rpm. Therefore, X-ray diffraction data was recorded at every revolution, only when the ball was passing along the width of the gauge volume. The data acquired during each pass was summed, cumulatively, to produce the X-ray diffraction pattern.

To enable the synchronisation of the rotating shaft attached to the test bearing and the EDXD detector gate, a Hall sensor on the bearing rig was used to generate the gating signal. A transistor was attached to the fixed outer raceway of the test bearing and a magnet was fixed to the bearing cage. Every time the transistor passed over the magnet a signal was generated which was passed through an oscilloscope to be conditioned. The conditioned triggering signal was used as an input into a National Instrument function generator which provided a square pulse triggering Transistor-Transistor Logic (TTL) signal indicating that the ball is in position; the TTL signal was fed into the ZEBRA signal processing equipment (developed by Diamond Light Source [19]) at 10kHz; ZEBRA operated the gate on the EDXD detector. To finely tune the ZEBRA signal, high-speed radiography was used which is described in the next section. The gate pulse phase lag and width was determined to be 23 milliseconds and 2 milliseconds respectively when the shaft was rotating at 150 rpm. This means that X-ray signal accumulation only over 2 milliseconds, which corresponded to the period during which the ball was in position, took place at every revolution.

## 2.3   High-speed radiography

Before carrying out the EDXD dynamic experiment, high-speed radiography was performed while the test bearing was running at 150 rpm. This was to confirm the triggering system provided the correct signal for the EDXD detector gate, only when the ball was in position. A scintillator was positioned behind the outer raceway of the test bearing, in the area that was to be examined by EDXD, to convert the X-rays transmitted through the bearing to visible light [20]. The scintillator was imaged via a mirror and a lens using a Vision Research Miro 310M CMOS camera with a resolution of 1280 × 800 pixels at 3200 frames per second. The trigger from the Hall Sensor on the bearing was used as an event marker in the high-speed X-ray video radiography recorded by the camera. The high-speed video was used to see where the ball position was when the trigger signal was received. Knowing the precise inter-frame time from the camera, the phase lag required for the EDXD gating signal was

calculated. The lag was programmed into the beamline's ZEBRA system, and finally another video was recorded to confirm that the ball was in the correct position when the trigger signal was received. A video was also recorded at the end of the experiment which confirmed consistency throughout the experiment. A high speed X-ray video is included in the supplementary electronic material to this paper. An example of single frame radiograph is shown in Figure 1b .

## 2.4 Strain measurement

### 2.4.1 X-ray diffraction

Measurements using X-ray diffraction are based on the Bragg's law [21]:

$$2d^{hkl}sin\theta = n\lambda \qquad \qquad \text{Eq. 2.1}$$

where $d^{hkl}$ is the characteristic distance between crystallographic planes (i.e. lattice spacing), specific to the *hkl* Miller indices, $\theta$ is the X-ray beam incidence angle, *n* is the order of reflection and $\lambda$ is the X-ray wavelength.

Monochromatic powder diffraction, a well-established and documented method, measures the distance between the lattice planes (i.e. $d^{hkl}$) by shining an incident beam of photons with a known wavelength onto a polycrystalline material. The present study is based on a less frequently used Energy Dispersive X-Ray Diffraction method. In EDXD the X-ray beam does not have a single value wavelength. To deduce the lattice spacing in this case, $\theta$ is fixed whilst $\lambda$ varies. Thus, only diffracted beam at a specific angle is recorded by the EDXD detector; fixed at $2\theta$ =5° at the JEEP beamline [22]. This is achieved with a sample slit fixed between the sample and the EDXD detector. The rationale for choosing the diffraction angle $2\theta$ =5° has been given elsewhere [23]. The energy range at JEEP is 50 keV to 150 keV [22].

The JEEP beamline uses a Canberra custom made EDXD detector which is cooled cryogenically. It is a high-purity germanium (Ge) detector with 23 detector elements (0 to 22) arranged in a semi-circular array with 8.18° angular spacing. The angular positions of the detector elements correspond to a rotation about the incident beam direction, denoted the azimuthal angle, $\varphi$ (see Figure 1d). The diffraction signal from the sample is therefore collected as a function of azimuthal angle. Detector element number 0 corresponds to an azimuthal angle at mean angle of $\varphi = 0°$, detector element number 1 at $\varphi = 8.18°$, detector element number 2 at $\varphi = 16.36°$ and so on, up to detector element number 22 at $\varphi = 180°$. Each germanium semiconductor spectroscopic detector element counts photons as a function of their energy *E*. Therefore, the intensity of the diffracted beam as a function of energy is measured by each detector element. Bragg's law can be rewritten to calculate lattice spacing via:

$$d^{hkl} = \frac{hc}{2\,Esin(\theta)} \qquad \qquad \text{Eq. 2.2}$$

Where *h* is Planck's constant and *c* is the speed of light.

### 2.4.2 Static strain measurement

Before the dynamic EDXD experiment, i.e. test bearing rotating, a static EDXD experiment was performed to compare the contact strains in the fixed outer raceway

under similar loads in the dynamic conditions. The bearing test rig was fixed onto the experimental stage in the External Experiment Hutch (EH2) of the JEEP beamline. Figure 1c shows the experimental setup schematically. The rotation axis of the bearing was aligned along the direction of the incident X-ray beam; i.e. $Z$-axis shown in Figure 1c. Precise alignment of the bearing with the X-ray beam was confirmed using the high-speed X-ray imaging camera as discussed in section 2.3 in detail.

In the EDXD setup, the diffracted beams are collimated by a semi-annular slit array mounted on the entrance window of the detector (the detector slit) and a second semi-annular slit with a fixed gap mounted close behind the sample (the sample slit). The sample slit together with the size of the collimated incident beam define the three-dimensional gauge. In this study, an incident beam size $0.25 \times 0.25$ mm$^2$ was used, with a 0.15 mm sample slit and 0.2 mm detector slit. Details of calculating the gauge volume can be found elsewhere [24] and therefore are not repeated here. Using this setup, the gauge length, was calculated to be 6.4 mm. The distance between the specimen and the detector was 2215 mm.

Three different loadings, $p$, were used while the test bearing was stationary: $p$ =0, 710 N, and 1420 N. The loads were applied by hanging a deadweight on the lever attached to the bearing housing supported by a pivot as described in section 2.1 and shown in Figure 1a. X-ray diffraction patterns were collected from 11 equally distanced points, along the $Y$-axis, $A$ to $K$, shown in Figure 1a. The first point, denoted by $A$ in Figure 1a, measures the diffraction pattern averaged over the $0.25 \times 0.25 \times 6.4$ mm$^3$ gauge volume in the outer raceway of the test bearing, with its centre 125 μm from the point of the contact between the ball and the outer raceway along the $Y$-axis. A 125 μm interval was defined between each measurement point resulting in 125 μm overlap in each measurement gauge volume along the $Y$-axis. Therefore, the centre of the gauge volume of the next measuring point, $B$ in Figure 1a, was 250 μm from the point of contact between the ball and the outer raceway. The last measurement point, $K$, was 1.375 mm from the point of contact. For each point, X-ray data was collected for 120 seconds.

### 2.4.3 Dynamic strain measurement

The setup in the dynamic strain measurement was similar to that used in the static case. Note that the dynamic strain is the strain induced in the fixed raceway by the moving balls as the inner raceway of the test bearing rotates. As described in section 2.2, the diffraction signal in each germanium detector element were recorded for 2 milliseconds, corresponding to a 250 μm (the gauge volume width) ball travel at 150 rpm. An accumulated 20 seconds count time was used in the dynamic case. Five different loadings were considered: $p$ = 0, 710, 1180, 1420, and 2365 N, and diffraction patterns were collected. Measurements were carried out only at one point, $B$ (see Figure 1a, with its centre 0.250 μm from the point of contact; section 3.3 for the justification.

### 2.5 Material and microstructural characterisation

The test bearing's raceway was fabricated from SAE-AISI 52100 type steel, the composition of which is reported in Table 1. Following the diffraction experiment a sector of the outer raceway was characterised post-mortem. A section of the outer raceway of the test bearing, which was interrogated during the EDXD experiment, was cut using a precision saw, then the surface was prepared using progressively fine abrasive media and finishing with colloidal silica; enabling the observation of grain

size, morphology and texture. Electron Back-Scatter Diffraction (EBSD) was used, observing the surface perpendicular to the X-ray beam direction and parallel to the radial-circumferential plane of the bearing. A JEOL-6500F scanning electron microscope equipped with a TSL/EDAX OIM v6 system was used, operating with a beam current of 15 nA and an accelerating voltage of 20 keV. Data was acquired over an area 24 μm × 24 μm with a step size of 0.1 μm. Diffraction indexing was performed using the Hough method on 1000 × 1000 pixel images with a 2 ×2 camera binning.

The cut sector was also intended to be used as the strain free reference specimen, also known as the $d_0$ specimen [25]. The specimen was annealed after EBSD for 8 hours at 600ºC [26] to relieve any locked-in stress. The specimen was re-scanned with the EDXD detector at a later date, albeit with a re-aligned and re-calibrated system to collect the strain free lattice spacing.

## 2.6 *Finite element simulations*

In order to investigate the effects of possible misalignment of the force on the contact stress field in the outer raceway of the test bearing, a series of three-dimensional quasi-static elastic finite element (FE) simulations were performed. Abaqus Standard 6.14 finite element package was used to simulate the bearing with 250,000 8-node brick elements. Macromechanical properties of steel were Young's modulus, $E = 207$ GPa and Poisson's ratio $v = 0.3$ [27]. The bearing housing and the shaft were not simulated explicitly; instead they are resented by two rigid faces modelled using 10,000 rigid shell elements. Two reference points, each associated with the bearing housing and the shaft were defined. Movements of all six degrees of freedom (displacements along *X*, *Y*, and *Z* axes as well as rotations around them $R_x$, $R_y$, and $R_z$) of the nodes defining the rigid bodies, representing the bearing housing and the shaft, are identical to the movements of their respective reference points. Frictionless tangential and hard normal contact was defined between the bearing and the rigid elements. Nonlinear geometry was considered in the simulations as significant nonlinear geometry has been observed in the previous contact simulations [28].

For the simulations, the reference point associated with the shaft was fixed in all six degrees of freedom while the reference point associated with the bearing housing was fixed in $Z$, $R_x$, $R_y$, and $R_z$. To apply the load, an arbitrary displacement was assigned to the reference point associated with the bearing housing in the *X* and *Y* directions depending on the degree of misalignment (see section 4). Because the model is fully elastic, the reaction force recorded at the reference points has a linear relationship with the magnitude of the applied displacement.

# 3   Results and analysis

## 3.1 *EDXD*

Examples of the X-ray diffraction patterns are given in Figure 2a for static and dynamic (stroboscopic) tests. They show the intensity of diffracted beam as a function of energy in detector element number 11. Five ferrite peaks are detectable in the patterns associated with {110}, {200}, {211}, {220}, and {310} diffraction planes. The peaks that are not indexed are associated with fluorescence. They are coherent or incoherent scattering from the slits. It can be seen that the intensity of the peaks in the dynamic pattern is lower than those of the static case. This was expected as the count time in the static case was 120 seconds whereas the accumulative count

time in the dynamic case was 20 seconds. The change in the peak width in static and dynamic case is the result of averaging over a varying strain volume in time which takes place in dynamic test and not in static. The full width half maximum in static peak is 0.014 Å and for dynamic peak 0.032 Å.

The location of the peaks in an X-ray diffraction pattern, i.e. $d^{hkl}$, can be identified, each corresponding to a reflection plane defined by $hkl$ indices. If the diffraction patterns before and after a deformation are recorded, the micromechanical strain for each diffraction plane, $\varepsilon^{hkl}$, is calculated by:

$$\varepsilon^{hkl} = \frac{d^{hkl} - d_0^{hkl}}{d_0^{hkl}}$$

Eq. 3.1

This process can be repeated for each of the 23 detector elements, providing micromechanical strain in every $8.18^{\circ}$ from $\varphi = 0^{\circ}$ to $\varphi = 180^{\circ}$. Figure A1 illustrates the orientation of the detector and the detector element number in correlation with the azimuth $\varphi$, the scattering vector, $\theta$, and diffraction planes $hkl$. By neglecting the small out-of-plane component of the scattering vector, the micromechanical strain calculated from the patterns along a known azimuth $\varphi$ can be expressed as [29]:

$$\varepsilon_\varphi^{hkl} = p_{xx}^{hkl}\sigma_{xx} + p_{xy}^{hkl}\sigma_{xy} + p_{yy}^{hkl}\sigma_{yy}$$

Eq. 3.2

where $p_{ij}^{hkl}$ are the stress factors and $\sigma_{ij}$ are the components of the two-dimensional macromechanical stress tensor in the coordinate system shown in Figure A1. The stress factors incorporate both the direction of the detector element (i.e. azimuth $\varphi$) and their corresponding elastic moduli $E^{hkl}$. Assuming perfect alignment of the beam and the sample coordinate systems the stress factors are [30]:

$$\varepsilon_\varphi^{hkl} = \frac{1}{2}S_2^{hkl}\left(\sigma_{xx}\cos^2\varphi + \sigma_{xy}\sin(2\varphi) + \sigma_{yy}\sin^2\varphi\right) \\ + S_1^{hkl}\left(\sigma_{xx} + \sigma_{yy}\right)$$

Eq. 3.3

$$p_{xx,\varphi}^{hkl} = S_1^{hkl} + \frac{1}{2}S_2^{hkl}\cos^2\varphi$$

$$p_{xy,\varphi}^{hkl} = \frac{1}{2}S_2^{hkl}\sin(2\varphi)$$

$$p_{yy,\varphi}^{hkl} = S_1^{hkl} + \frac{1}{2}S_2^{hkl}\sin^2\varphi$$

where diffraction elastic constants (also known as X-ray elastic constants) for a $hkl$ diffraction plane $S_1^{hkl}, \frac{1}{2}S_2^{hkl}$ are defined as [29]:

$$S_1^{hkl} = -\nu^{hkl}/E^{hkl}$$

$$\frac{1}{2}S_2^{hkl} = (1 + \nu^{hkl})/E^{hkl}$$

Eq. 3.4

A comprehensive review of $\varepsilon_\varphi^{hkl}$ conversion to $\sigma_{ij}$ can be found in reference [31] and therefore is not repeated here. It should be noted that a constant external load or a steady state internal residual stress field can induce different levels of micromechanical strains in different diffraction planes. The strain in a diffraction plane is a function of the elastic modulus of the diffraction plane and the boundary conditions of the grain, i.e. the orientation of the surrounding grains and their elastic

moduli. Therefore, the micromechanical strains measured at different azimuths for different diffraction planes, $\varepsilon_{\varphi}^{hkl}$, do not necessarily satisfy macroscopic mechanics' compatibility equations. If the micromechanical strains are converted into the macromechanical stress field, however, equilibrium is satisfied and the stress calculated at a particular azimuth can be converted to a different azimuth by a simple use of the stress transformation equations.

Finally, it should be noted that the residual stresses that are locked in the component during the manufacturing processes can be measured by comparing the diffraction patterns of a strain free specimen and the patterns obtained from the component [25] without any applied load. The strain free sample is commonly known as a $d_0$ specimen and the methods for its preparation is discussed in details in reference [25].

Peak search and fitting was performed using a scale-space representation (ridge search) method, by a Laplacian of Gaussian kernel, followed by non-linear least squares refinement using a Gaussian peak profile [32]. Five peak positions in all cases was identified for the 3 loading conditions ($p$ = 0, 710, and 1420 N) at 11 points, *A-K*, in the static experiment and 5 loading conditions ($p$ = 0, 710, 1180, 1420, and 2365 N) at one point, *B*, in the dynamic test. The micromechanical strain developed for each reflection could be calculated using Eq. 3.1 for 23 azimuths $\varphi = 0°$ to $\varphi = 180°$ at 8.18° intervals. The free strain lattice parameters, i.e. $d_0^{hkl}$, were required to calculate the residual stress. As discussed in section 2.5, it was intended to use the X-ray diffraction patterns obtained from the strain free, cut, and annealed $d_0$ specimen to measure $d_0^{hkl}$. However, because the $d_0$ specimen could not be scanned at the same time as the test bearing and EDXD, measurements were carried out on a re-aligned and re-calibrated detector, the measured $d_0^{hkl}$ values from the $d_0$ specimen were therefore deemed invalid for strain calculations and therefore the residual stress could not be measured. For strain measurements in the static and dynamic tests, the strain free lattice parameter for each reflection was determined by introducing an in-plane deviatoric stress, $\sigma_{dev}$, and a pseudo-hydrostatic stress $\sigma_{ph}$, the details of this assumption have been discussed elsewhere [29]:

$$\varepsilon_{\varphi} = \frac{\bar{d}_{\varphi}^{hkl} - d_0^{hkl}}{d_0^{hkl}} = (p_{xx} - p_{yy})\sigma_{dev} + p_{xy}\sigma_{12} + p_{ph}\sigma_{ph} \qquad \text{Eq. 3.5}$$

where

$$p_{ph} = \frac{1}{2}S_2 + 3S_1 \qquad \text{Eq. 3.6}$$

where $\bar{d}_0^{hkl}$ is an approximation of the strain free lattice spacing. The pseudo-hydrostatic stress is dominated by the portion from an incorrect $d_{\varphi}^{hkl}$ but potentially includes any hydrostatic portion of the in-plane stress. The pseudo-hydrostatic stress ($\sigma_{ph}$) is defined as the summation of normal stresses divided by 3 $\left(\frac{\sigma_{xx} + \sigma_{yy} + \sigma_{zz}}{3}\right)$, which quantifies the dilatation of the diffraction ring whereas the deviatoric stress, $\sigma_{dev}$, (i.e. $\sigma_{xx} - \sigma_{yy}$) quantifies the distortion of the ring.

After obtaining an average $\sigma_{ph}$ for each lattice plane and for all specimens, the strain free lattice spacing $d_0^{hkl}$ for each reflection was calculated according to:

$$d_0^{hkl} = d_\varphi^{hkl}\left(1 - p_{ph}\sigma_{ph}^{hkl}\right) \qquad \text{Eq. 3.7}$$

Inspection of the strain values at boundary conditions (i.e. traction free surface) and equilibria suggested the approximation is sufficient. No geometry dependence was observed in the measured $d_0^{hkl}$ value for all detector elements validating the appropriateness of the assumed $d_0^{hkl}$. However, the residual stress of the specimen could not be evaluated as only the physically meaningless pseudo-hydrostatic stress could be measured from the $d_0$ sample by this method. The pseudo-hydrostatic stress measured from the $d_0$ specimen was found to be a constant value (within 2.5%), indicating proof for the suitable approximation.

As an example, the micromechanical strain distribution calculated in the dynamic condition at the load $p$ = 1420 N is shown in Figure 2b. The root mean square strain for all diffraction planes in all azimuths at $p$ = 0 N for static test is calculated to be 60 $\mu\varepsilon$. Similarly, the root mean square strain of all diffraction planes in all azimuths at $p$ = 0 N for dynamic test is calculated to be 230 $\mu\varepsilon$. These was deemed to be the accuracy with which the *hkl* micromechanical strains were measured in static and dynamic cases respectively.

## 3.2 Microstructure

An EBSD inverse pole figure map of the cut bearing steel section is shown in Figure 3a. The figure shows that the grain size of the material is ~1 μm. The obvious randomness of the colours, each indicating the orientation of the indexed grain, in the map shows that there is no texture in the material. The larger green region observed in the plot is an agglomerated cluster of grains, all orientated similarly. An orientation distribution function (ODF) of this data, shown in Figure 3b, plots the orientation of each data point on a pole figure. The points are distributed quite uniformly, indicating no preferred texture is present. This is an important finding as both the bulk macroscopic response and the accumulation of lattice strains are known to be affected by texture [11, 33]. As such, the validity of the analysis described in the section 3.3 depends on random grains from which the micromechanical strains have been measured.

## 3.3 Macroscopic stress calculation

The low diffraction angle of EDXD experiments means the scattering vectors essentially lie within a single plane. This allows for the determination of the in-plane components of stress in a single measurement [34], however, out-of-plane stresses cannot be determined. For the interrogated gauge volume, whose 2D plane strain macromechanical stress tensor can be defined fully by three independent components, 23×5 (23 detector elements/azimuths, 5 diffraction peaks) micromechanical strains were calculated. In order to convert the micromechanical strains to a single macromechanical stress tensor, the following equations system was used:

$$\{\boldsymbol{\varepsilon}\}_{1\times115} = \{\boldsymbol{\sigma}\}_{1\times3}[\boldsymbol{p}]_{3\times115}$$

$$\{\boldsymbol{\varepsilon}\} = \{\varepsilon_0^{110} \quad \varepsilon_0^{200} \quad \varepsilon_0^{211} \quad \varepsilon_0^{220} \quad \varepsilon_0^{310} \quad \varepsilon_1^{110} \quad ... \quad \varepsilon_{22}^{310}\} \qquad \text{Eq. 3.8}$$

$$\{\boldsymbol{\sigma}\} = \{\sigma_{xx} \quad \sigma_{xy} \quad \sigma_{yy}\}$$

$$[\boldsymbol{p}] = \begin{bmatrix} p_{xx,0}^{110} & p_{xx,0}^{200} & p_{xx,0}^{211} & p_{xx,0}^{220} & p_{xx,0}^{310} & p_{xx,1}^{110} & \cdots & p_{xx,22}^{310} \\ p_{xy,0}^{110} & p_{xy,0}^{200} & p_{xy,0}^{211} & p_{xy,0}^{220} & p_{xy,0}^{310} & p_{xy,0}^{110} & \cdots & p_{xy,22}^{310} \\ p_{yy,0}^{110} & p_{yy,0}^{200} & p_{yy,0}^{211} & p_{yy,0}^{220} & p_{yy,0}^{310} & p_{yy,0}^{110} & \cdots & p_{yy,22}^{310} \end{bmatrix}$$

where the unknowns are 2D stress tensor with three components, $\{\boldsymbol{\sigma}\}_{1\times3}$, while the strain values, $\{\boldsymbol{\varepsilon}\}_{1\times115}$, with 115 values are measured and the stress factor matrix, $[\boldsymbol{p}]_{3\times115}$, with 345 components is constructed using Eq. 3.3. In the strain matrix $\{\boldsymbol{\varepsilon}\}$ the subscript denotes detector element number/azimuth and superscript denotes the diffraction plane. For example, $\varepsilon_0^{110}$ is the micromechanical strain measured from the detector number 0 (see Figure 1c for detector element numbers) at {110} diffraction plane. In the stress factor matrix, $[\boldsymbol{p}]$, the first subscript denotes the direction of stress, the second the detector element number/azimuth and the superscript the diffraction plane. For example, $p_{xy,2}^{220}$ is the stress factor for $\sigma_{xy}$, in the second detector on {220} plane.

Diffraction elastic constants for ferrite diffraction planes are well documented [35] and therefore there was no need to measure them; they were obtained from ISODEC software without texture [36] and are reported in Table 2. Eq. 3.8 describes an over-determined system of linear equations. Therefore, the stress tensor that best fits Eq. 3.8 was calculated using a simple optimisation technique:

$$\{\boldsymbol{\sigma}\}_{1\times3} = \{\boldsymbol{\varepsilon}\}_{1\times115}([p]^+)_{115\times3} \qquad \text{Eq. 3.9}$$

where $([p]^+)_{115\times3}$ denotes the Moore-Penrose pseudo-inverse of $[p]_{3\times115}$. The components of the static stress tensor, $\sigma_{ij}^s$, at two different loads ($p$= 710, and 1420 N) for the static case at 11 locations in the $Y$ direction from the contact point (see section 2.4.2) were calculated and are shown in Figure 4a. Single peak shift analysis at the time of the experiment showed an increase between strains measured in points A and B, the increase was interpreted as the gauge volume having a partial overlap with the ball. It was therefore judged more appropriate to measure the critical dynamic strains at point $B$. Therefore, the dynamic stresses, $\sigma_{ij}^d$, while the bearing was rotating, were calculated at point $B$ using a similar procedure to the one carried out for the static condition. The centre of the gauge volume at point $B$ was at 0.250 μm from the contact point. The dynamic stresses were calculated at 5 loading conditions ($p$ =0 , 710, 1180, 1420, and 2365 N), results of which are plotted in Figure 4b. Note that the error bars shown in Figure 4 represent the variation between the stresses calculated from different lattice planes.

## 3.4 Finite element results

Ten finite element models with an arbitrary 0.1 mm vertical displacement ($V_y$) and varying horizontal displacements ($V_x$ from 0 to 0.1 in 10 steps), representing the experimental misalignment, were analysed. The displacements were applied to the reference point associated with the rigid body representing the bearing housing. Although the model had linear elastic material properties, nonlinearity was observed in volumes located closer than 100 μm to the contact point. This was nonlinearity in the relationship between the applied load and the stress field. This is due to high levels of deformation at the contact point and is an indication that adopting a nonlinear geometry option in the simulation was necessary.

A contour of the compressive stress component $(-\sigma_{yy})$ of stress tensor at the middle of the 2ms trigger at $p = 1420$ N is shown in Figure 5a. The gauge volume is superimposed on the contour to show the area over which the experimental averaging was carried out. It is important to note that the spatial resolution of the data in the FE simulation and in the experiment are different. The components of the stress tensor averaged at the centre of each element can be extracted from the FE results but the volume of the finite elements in the model are much smaller than the gauge volume used in the experiment. Adopting such small elements were necessary and were determined via a straight forward mesh dependency study that was carried out using the reaction force at the reference point as the target value which should converge to a single value as the element sizes were reduced step-wise. It was, therefore, important to extract an average stress value over a volume similar to that which was used during the experimental measurements.

To this end, the average values of the stress tensor components at the centre of each element were extracted from the simulation as well as the coordinates of each node that formed the element. An in-house Matlab® code was developed to take a weighted average of stresses, with respect to each element's volume, over a volume that corresponded to the gauge volume used in the experiment at points corresponding to $A$ to $K$. This allows a direct comparison between the EDXD measured stress field and that calculated by the FE simulation.

By using the finite element results, the level of 'blurring' caused by both time and volume averaging during the experiment could be quantified. Figure 5b shows the variation of the compressive stress over time at the point of contact between the ball and the raceway. Also shown in the figure is the variation of the compressive stress over the time averaging which was resulted from the 2 ms width of the trigger. The ratio of the averaged stress over 2ms over the maximum compressive stress is 0.25 indicating a 75% blurring as a result of such averaging. Figure 5c shows the variation of the compressive stress along the 6.7 mm gauge length. It shows that the average compressive stress over the gauge length is 37% of the maximum stress which is 63% 'blurring' in the measurement.

The difference between the magnitude of von-Mises stress at point $B$ between FE simulations and experimental measurement of static experiment at $p = 1420$ N was calculated for different levels of misalignment (i.e. horizontal $V_x$ disablement). By interpolating the differences as a function of $\alpha = atan(V_x/V_y)$, the minimum difference was observed at $\alpha = 3^o$ indicating a small experimental misalignment in applied load which could have been resulted from the pivot. A finite element model with the optimised misalignment was performed whose results are reported below.

Figure 6a and b show the difference between the stress tensor components measured in static case at $p = 710$ N and $p = 1420$ N. A general good agreement can be seen between the FE and experiment. However, the biggest component of stress, i.e. $\sigma_{yy}^s$, shows the best agreement and the least correlation is observed between the shear stresses. A trend can also be seen, in particular in Figure 6b, that the larger the stress (the closer to the contact point) is, the better the agreement between FE and experiment. For the dynamic stress measurements, the static FE stress in $y$ direction, $\sigma_{yy}^s$, shows a good agreement with the dynamic stress measurement, $\sigma_{yy}^d$. Considering the relatively low speed of the shaft rotation (150 rpm) this is expectable and in agreement with previous studies [37].

# 4 Discussion

It is clear that the data quality of diffraction reflections obtained during static loading was much higher than the dynamic case, providing comparably higher peak position fit accuracy. Counting statistics were better for the static case. However, this novel experiment showed the opportunities that high-energy synchrotron beamlines such as JEEP provide in measuring macroscopic dynamic stress fields.

The root mean square of stress tensor components at $p = 0$ N in the static case was calculated: $\sigma_{xx}$= 7, $\sigma_{yy}$= 12, $\sigma_{xy}$= 5 MPa which is considered to be the accuracy of the stress calculation technique in the static condition. The root mean square of stress tensor components at $p$ =0 N in the dynamic case was $\sigma_{xx}$ = 19, $\sigma_{yy}$ = 14, and $\sigma_{xy}$= 10 MPa representing the accuracy of the stress calculation in dynamic case. Unsurprisingly, the accuracy in the static case is higher.

It can be seen in Figure 4 that the stress components calculated at the same external load in static and dynamic conditions are comparable. The highest stress component, i.e. stress in Y direction, $\sigma_{yy}$, at point B with a load $p = 1420$ N is $\sigma_{yy}^{s}$= -84±12 MPa in the static and $\sigma_{yy}^{d}$ = -80±14 MPa in the dynamic conditions. For $p = 710$ N, there is less agreement between the static stress $\sigma_{yy}^{s}$= -60±12 and dynamic stress $\sigma_{yy}^{d}$ = -67±14. It could be argued that the confidence in the measured stress, particularly in dynamic case, grows as the stress level increases as the signal to noise ratio of the obtained diffraction patterns improves, resulting in more accurate identification of the peak position and consequently, the stress calculation.

The static finite element stress along the Y-axis at $p = 710$ N is $\sigma_{yy}$= -81 MPa and at $p = 1420$ N, $\sigma_{yy}$= -58 MPa which is only a 3% different from the static experimental values; the difference increases to 15% in the case of dynamic experiment. However, it could be argued that there is a misalignment of the applied load on the bearing housing through the pivot with respect to a pure vertical direction along the Y-axis. FE simulation showed that considering a 3° misalignment the difference between FE results and dynamic experiment is minimised to 12%. All FE values reported here are averaged over time and distance similar to that measured experimentally.

Figure 4a shows that the algebraic value of the stress components decrease as the distance from the contact point increases. The stress tensor components plateau after approximately 1 mm from the contact point to a uniform far field stress. The stress components at the first point of the profile, i.e. point $A$ whose centre is at $y$=125 µm, however, do not follow the decreasing trend. This is consistent with the FE simulation results. During the experiment the deviation observed in the measurement was interpreted as the gauge volume being partially filled with the ball. Therefore, the decision was made to measure the dynamic strain at point $B$. FE simulation shows that the deviation was, with hindsight, expectable and the gauge volume was not partially filled but was fully contained in the fixed outer raceway.

Figure 4b shows that the four compressive stresses in dynamic case, $\sigma_{yy}^{d}$, at loads $p = 710, 1180, 1420$, and 2365 N have a linear relationship with their respective applied loads with a goodness of fit $R^2$= 0.9851. Other stress components, $\sigma_{xx}^{d}$ and $\sigma_{xy}^{d}$ , are within the noise level of the technique and such a uniform trend cannot be observed. Thus, to compare all the results, the stress values could be normalised with respect to the applied load:

$$S_{ij} = \frac{\sigma_{ij}}{p/_{W \times R_o}}$$ <div align="right">Eq. 4.1</div>

where $S_{ij}$ is the normalised stress, $\sigma_{ij}$ is the stress tensor component, $p$ is the applied force, $W$ is the bearing width (2 inches or 25.6 mm), and $R_o$ is the bore radius (2.875 inches or 73 mm). Figure 7a, b, and c show the normalised compressive ($S_{yy}$), horizontal ($S_{xx}$), and shear ($S_{xy}$) stress components. Each individual static and stroboscopic measurements are illustrated in the plots by symbols: circular for stroboscopic and square for static. It can be seen that the uncertainty in the stroboscopically calculated stresses are much bigger than those that were calculated from the static tests. This is due to the uncertainty calculated from fitting the stress field to 5 diffraction peaks at all 23 detector elements. The FE results are also shown in the figures with a continuous line. It can be observed in the figure that throughout the stress profiles, static normalised compressive and horizontal stress components show a good agreement with that of the finite element model. Close to the contact point (up to 0.5 mm), the shear stress shows a good correlation between FE and experiment but after 0.5mm, significant deviation between the two methods is observed.

## Concluding remarks

- The contact micromechanical static strain in a fixed outer raceway of a bearing was successfully measured along a radial profile at 11 points for two levels of external loads by energy dispersive X-ray diffraction technique. The dynamic strain, i.e. when the bearing was rotating at 150 rpm, was also measured at a single point on the fixed outer raceway of the bearing at five levels of external load.

- The components of the macroscopic 2D plane strain stress tensor were extracted from the measured micromechanical strains at different diffraction planes.

- Good correlation was observed between the stress tensor components measured in static and dynamic cases and both agreed well with the finite element results, increasing the confidence in the stroboscopic stress measurement.

- Having established the confidence in the stroboscopic strain measurement, future in-situ experiments are being designed to investigate crack initiation in the bearing raceway in real-time. The dynamic measurements will also be used to verify the acousto-elastic measurements.

## Acknowledgement

# References

1.   Dwyer-Joyce RS, Drinkwater BW, Quinn AM (2001) The use of ultrasound in the investigation of rough surface interfaces. ASME JOURNAL OF TRIBOLOGY 123:8–16.

2.   Motions and Control NSK (2009) Technical Report. CAT No E728

3.   Quinn AM, Drinkwater BW, Dwyer-Joyce RS (2002) The measurement of contact pressure in machine elements using ultrasound. ULTRASONICS 37:495–502.

4.   Dwyer-Joyce RS, Drinkwater BW (2003) The measurement of lubricant-film thickness using ultrasound. PROCEEDINGS OF THE ROYAL SOCIETY A-MATHEMATICAL PHYSICAL AND ENGINEERING SCIENCES 459:957–976.

5.   Ya M, Marquette P, Belahcene F, Lu J (2004) Residual stress in laser welded aluminium plate by use of ultrasonic and optical methods. MATERIALS SCIENCE AND ENGINEERING: A 382:557–564.

6.   Lopez-Crespo P, Mostafavi M, Steuwer A, Kelleher JF, Buslaps T, Withers PJ (2016) Characterisation of overloads in fatigue by 2D strain mapping at the surface and in the bulk. Fatigue & Fracture Of Engineering Materials & Structures In press:1–9.

7.   Santisteban JR, Daymond MR, James JA, Edwards L (2006) ENGIN-X: A third-generation neutron strain scanner. JOURNAL OF APPLIED CRYSTALLOGRAPHY 39:812–825.

8.   Daymond MR, Withers PJ (1996) A new stroboscopic neutron diffraction method for monitoring materials subjected to cyclic loads: thermal cycling of metal matrix composites. Scripta Materialia 35:717–720.

9.   Eckold G, Gibhardt H, Caspary D, Elter P, Elisbihani K (2009) Stroboscopic neutron diffraction from spatially modulated systems. ZEITSCHRIFT FÜR KRISTALLOGRAPHIE - CRYSTALLINE MATERIALS 218:144–153.

10.  Feuchtwanger J, Lazpita P, Vidal N, Barandiaran JM, Gutierrez J, Hansen T, Peel M, Momdelli C, O'Handley RC, Allen SM (2008) Rearrangement of twin variants in ferromagnetic shape memory alloy–polyurethane composites studied by stroboscopic neutron diffraction. JOURNAL OF PHYSICS: CONDENSED MATTER 20:104247.

11.  Collins DM, Mostafavi M, Todd RI, Connolley T, Wilkinson AJ (2015) Time resolved X-ray diffraction during biaxial deformation of sheet steel - Prat I: Proportional loading. ACTA MATERIALIA 90:46–58.

12.  Baimpas N, Drakopoulos M, Connolley T, Song X, Pandazaras C, Korsunsky AM (2013) A feasibility study of dynamic stress analysis inside a running internal combustion engine using synchrotron X-ray beams. JOURNAL OF SYNCHROTRON RADIATION 20:316–323.

13.  Petitgrand S, Yahiaoui R, Danaie K, Bosseboeuf A, Gilles JP (2001) 3D measurement of micromechanical devices vibration mode shapes with a stroboscopic interferometric microscope. OPTICS AND LASERS IN

ENGINEERING 36:77–101.

14. Podolsky R, Onge RST, Yu L, Lymn RW (1976) X-ray diffraction of actively shortening muscle. PROCEEDINGS OF NATIONAL ACADEMY OF SCIENCE USA: BIOPHYSICS 73:813–817.

15. Wulff M, Schotte F, Naylor G, Bourgeois D, Moffat K, Mourou G (1997) Time-resolved structures of macromolecules at the ESRF: Single-pulse Laue diffraction, stroboscopic data collection and femtosecond flash photolysis. NUCLEAR INSTRUMENTS & METHODS IN PHYSICS RESEARCH SECTION A-ACCELERATORS SPECTROMETERS DETECTORS AND ASSOCIATED EQUIPMENT 398:69–84.

16. Harrison RJ, Redfern SAT, Buckley A, Salje EH (2004) Application of real-time, stroboscopic x-ray diffraction with dynamical mechanical analysis to characterize the motion of ferroelastic domain walls. JOURNAL OF APPLIED PHYSICS 95:1706–1717.

17. Baimpas N, Drakopoulos M, Connolley T, Song X, Pandazaras C, Korsunsky AM (2013) A feasibility study of dynamic stress analysis inside a running internal combustion engine using synchrotron X-ray beams. JOURNAL OF SYNCHROTRON RADIATION 20:1–8.

18. Brömmelhoff K, Henze S, Gerstenberger R, Fischer T, Schell N, Uhlmann E, Reimers W (2013) Space resolved microstructural characteristics in the chip formation zone of orthogonal cut C45E steel samples characterized by diffraction experiments. Journal of Materials Processing Technology 213:2211–2216.

19. Cobb T, Chernousko Y, Uzun I, Light D (2014) ZEBRA : A FLEXIBLE SOLUTION FOR CONTROLLING SCANNING EXPERIMENTS. In: Proceedings of ICALEPCS2013. San Francisco, CA, USA, pp 736–739

20. Nikl M (2006) Scintillation detectors for x-rays. MEASUREMENT SCIENCE AND TECHNOLOGY 17:R37–R54.

21. Bragg WL (1914) XLII. The crystalline structure of copper. PHILOSOPHICAL MAGAZINE SERIES 6 28:355–360.

22. Drakopoulos M, Connolley T, Reinhard C, Atwood R, Magdysyuk O, Vo N, Hart M, Connor L, Humphreys B, Howell G, Davies S, Hill T, Wilkin G, Pedersen U, Foster A, De Maio N, Basham M, Yuan F, Wanelik K (2015) I12: The Joint Engineering, Environment and Processing (JEEP) beamline at Diamond Light Source. JOURNAL OF SYNCHROTRON RADIATION 22:828–838.

23. Korsunsky AM, Song X, Hofmann F, Abbey B, Xie M, Connolley T, Reinhard C, Atwood RC, Connor L, Drakopoulos M (2010) Polycrystal deformation analysis by high energy synchrotron X-ray diffraction on the I12 JEEP beamline at Diamond Light Source. MATERIALS LETTERS 64:1724–1727.

24. Rowles MR (2011) On the calculation of the gauge volume size for energy-dispersive X-ray diffraction. JOURNAL OF SYNCHROTRON RADIATION 18:938–941.

25. Withers PJ, Preuss M, Steuwer A, Pang JWL (2007) Methods for obtaining

the strain-free lattice parameter when using diffraction to determine residual stress. JOURNAL OF APPLIED CRYSTALLOGRAPHY 40:891–904.

26. Epp J, Surm H, Kovac J, Hirsch T, Hoffmann F (2011) Interdependence of distortion and residual stress relaxation of cold-rolled bearing rings during heating. METALLURGICAL AND MATERIALS TRANSACTIONS A: PHYSICAL METALLURGY AND MATERIALS SCIENCE 42:1205–1214.

27. Sommer C, Christ H-J, Mughrabi H (1991) Non-linear elastic behaviour of the roller bearing steel SAE 52100 during cyclic loading. ACTA METALLURGICA ET MATERIALIA 39:1177–1187.

28. Jackson RL, Green I (2005) A Finite Element Study of Elasto-Plastic Hemispherical Contact Against a Rigid Flat. Journal of Tribology 127:343.

29. He BB (2011) Two-dimensional X-ray diffraction. John Wiley & Sons Inc., Hoboken, NJ

30. Hauk V (1997) Structural and Residual Stress Analysis by Nondestructive Methods. ELSEVIER SCIENCE BV, Amstertam

31. Welzel U, Ligot J, Lamparter P, Vermeulen AC, Mittemeijer EJ (2005) Stress analysis of polycrystalline thin films and surface regions by X-ray diffraction. JOURNAL OF APPLIED CRYSTALLOGRAPHY 38:1–29.

32. Horne G, Peel MJ, Smith DJ (2013) Measurement of Elastic Follow-Up for Combined Applied and Residual Stresses. Proceedings of the ASME 2013 Pressure Vessels and Piping Conference

33. Hutchings MT, Withers PJ, Holden TM, Lorentzen T (2005) Introduction to the Characterization of Residual Stress by Neutron Diffraction. CRC Press

34. Horne G, Peel MJ, Hattingh DG, Connolley T, Hart M, Kelleher JF, Zhang SY, Smith DJ (2014) An experimental procedure to determine the interaction between applied loads and residual stress. MATERIALS SCIENCE FORUM 768–769:733–740.

35. Baczmański a., Wierzbanowski K, Haije WG, Helmholdt RB, Ekambaranathan G, Pathiraj B (1993) Diffraction Elastic Constants for Textured Materials — Different Methods of Calculation. CRYSTAL RESEARCH AND TECHNOLOGY 28:229–243.

36. Gnäupel-Herold T (2012) ISODEC: software for calculating diffraction elastic constants. Journal of Applied Crystallography 45:573–574.

37. Kraus J, Blech JJ, Braun SG (1987) In situ determination of rolling bearing stiffness and damping by modal analysis. JOURNAL OF VIBRATION, ACOUSTICS, STRESS, AND RELIABILITY IN DESIGN 109:235–240.

38. Muramoto S, Matsunaga H, Moriyama S, Endo M (2008) Crack size dependency of shear mode fatigue crack threshold in bearing steel. KEY ENGINEERING MATERIALS 385–387:449–452.

# Tables

**Table 1 – Chemical composition of SAE 51200 bearing bainitic steel** [38]

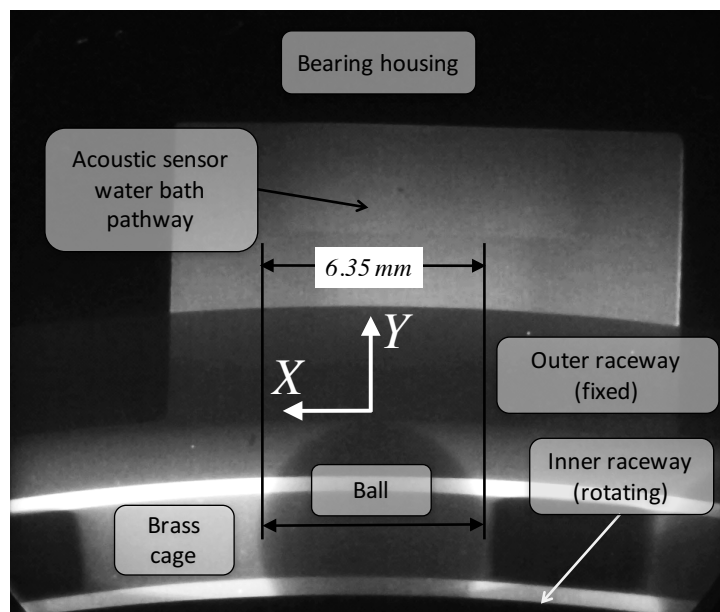| Element | Fe | C | Si | Mn | P | S | Cu | Ni | Cr | Mo |
|---------|----|---|----|----|---|---|----|----|----|----|
| wt.% | Balance | 0.98 | 0.16 | 0.38 | 0.12 | 0.06 | 0.12 | 0.07 | 1.39 | 0.02 |

**Table 2 – Diffraction Elastic Constants calculated by ISODEC software using macromechanical elastic modulus 207 GPa and Poisson ratio 0.3**

| Diffraction plane | | {110} | {200} | {211} | {220} | {310} |
|-------------------|---|-------|-------|-------|-------|-------|
| Diffraction elastic constants ($\frac{mm^2}{N} \times 10^6$) | $S_1$ | -1.29 | -1.94 | -1.29 | -1.29 | -1.71 |
| | $\frac{1}{2}S_2$ | 5.80 | 7.74 | 5.80 | 5.80 | 7.05 |

**Figures**



(a)



(b)

(c)



(d)
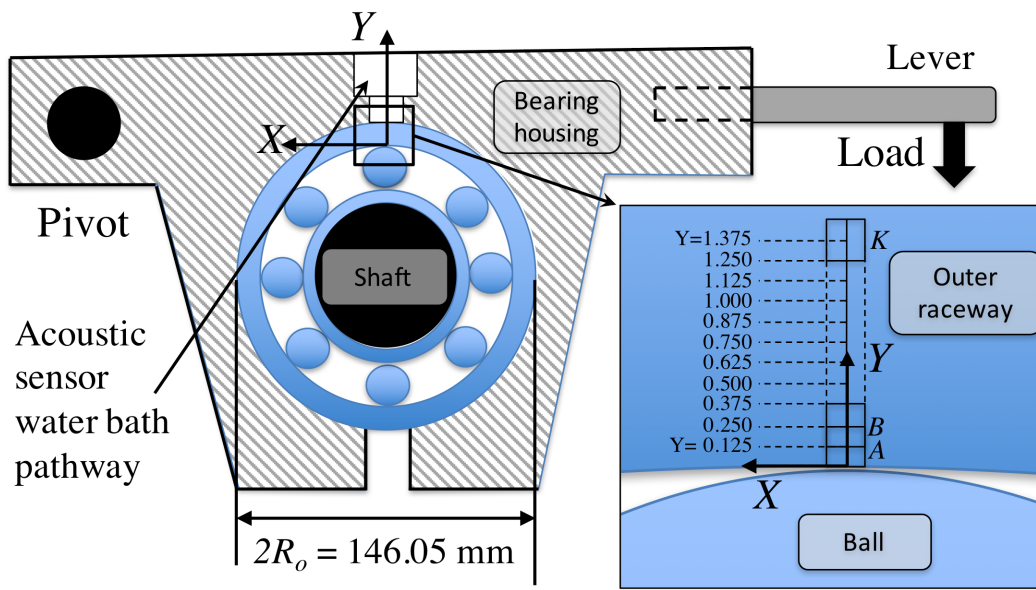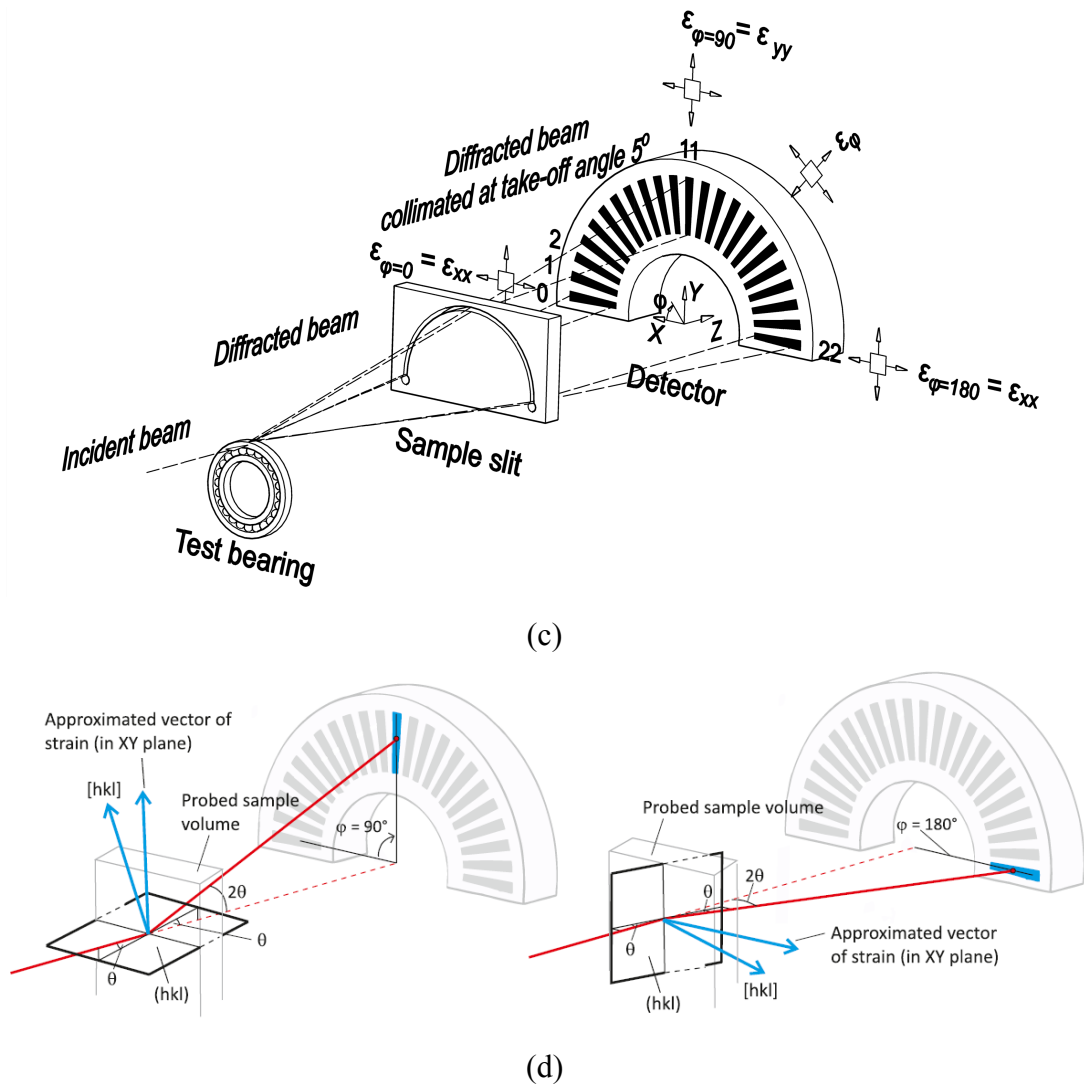
**Figure 1– (a) schematic of the test bearing in the bearing testing rig (b) single frame from high-speed X-ray radiography, part of the ball and the outer raceway can be seen (c) Schematic of the Energy Dispersive X-ray Diffraction experiment – distance between the sample slit and the detector was 1455 mm and the distance between the sample and the detector was 2210 mm (d) Diffraction geometry for two example detection positions at detector element number 11 (left) and detector element number 22 (right) - Note that the detector element numbers start from 0**
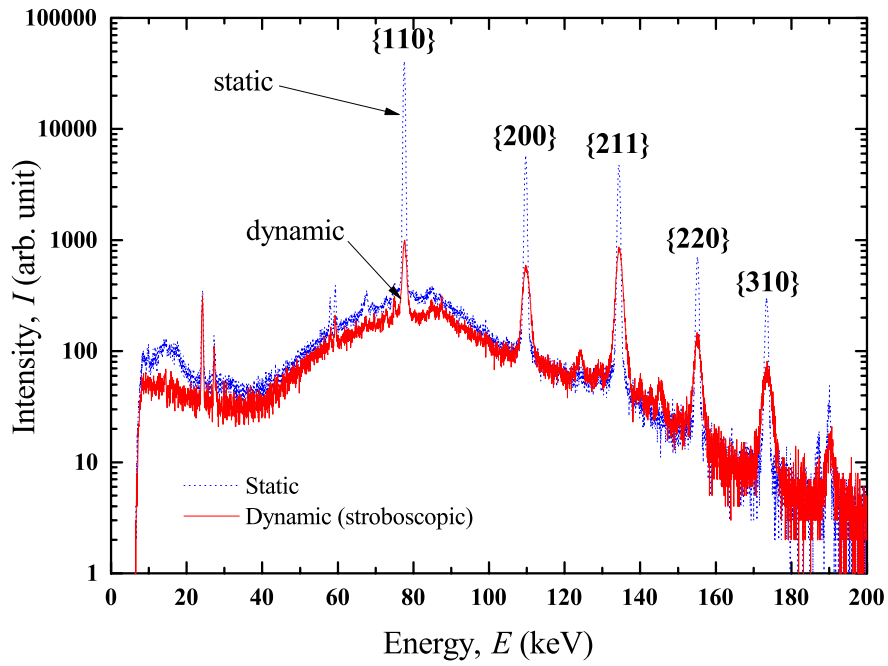
(a)
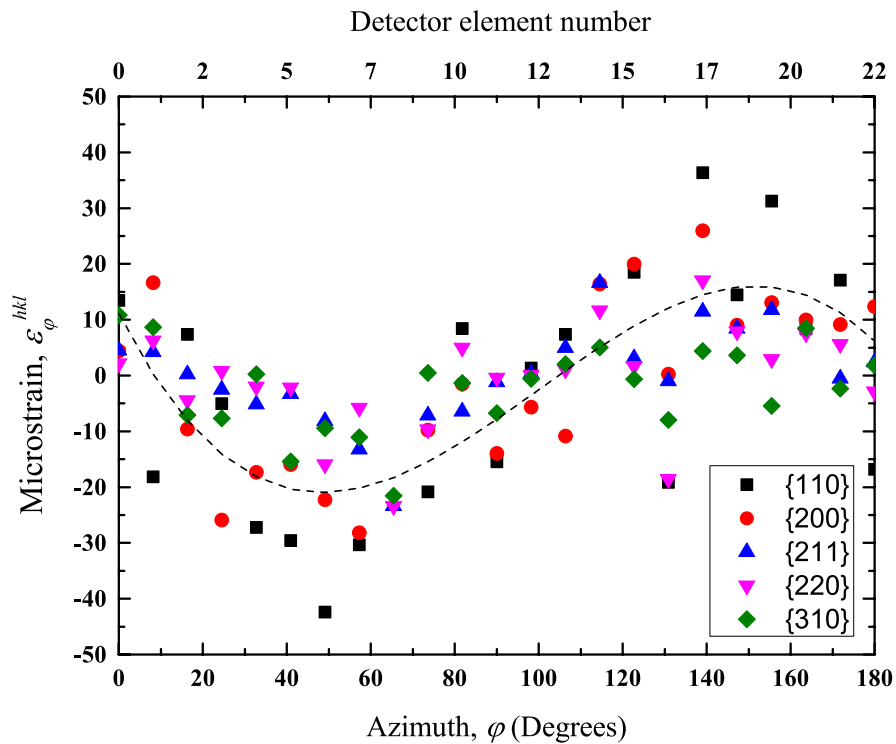


(b)

**Figure 2** –(a) Example of diffraction patterns in static and dynamic (stroboscopic) modes (b) example of the measured micromechanical strains associated with 5 diffraction planes along $\varphi$ = 0-180$^o$ azimuths at 8.18$^o$ intervals in dynamic mode at $p$ = 1420 N – the fitted stress field is shown as a dashed line
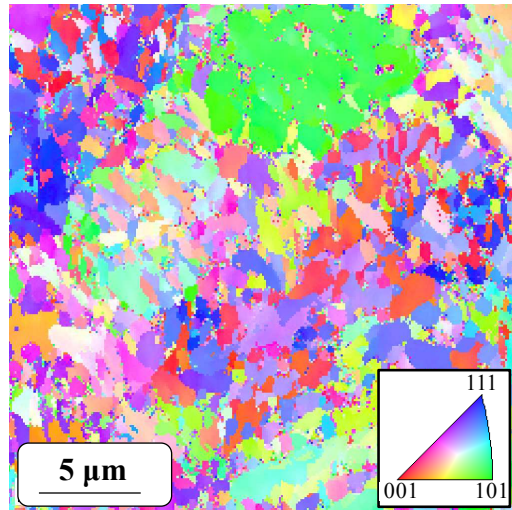
(a)
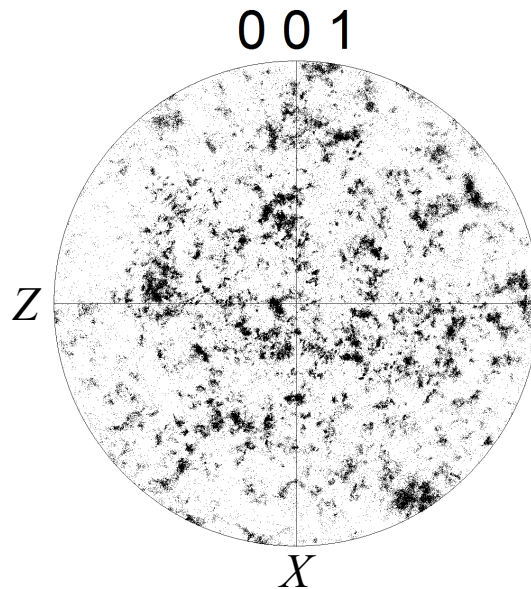


(b)

**Figure 3 – Microstructure (a) EBSD inverse pole figure map showing grain structure of bainitic steel with colours showing crystal directions; the randomness of the colour shows the lack of texture in the examined volume (b) orientation distribution function (ODF) map calculated from the EBSD map; the lack of texture is shown by randomness of the distribution.**
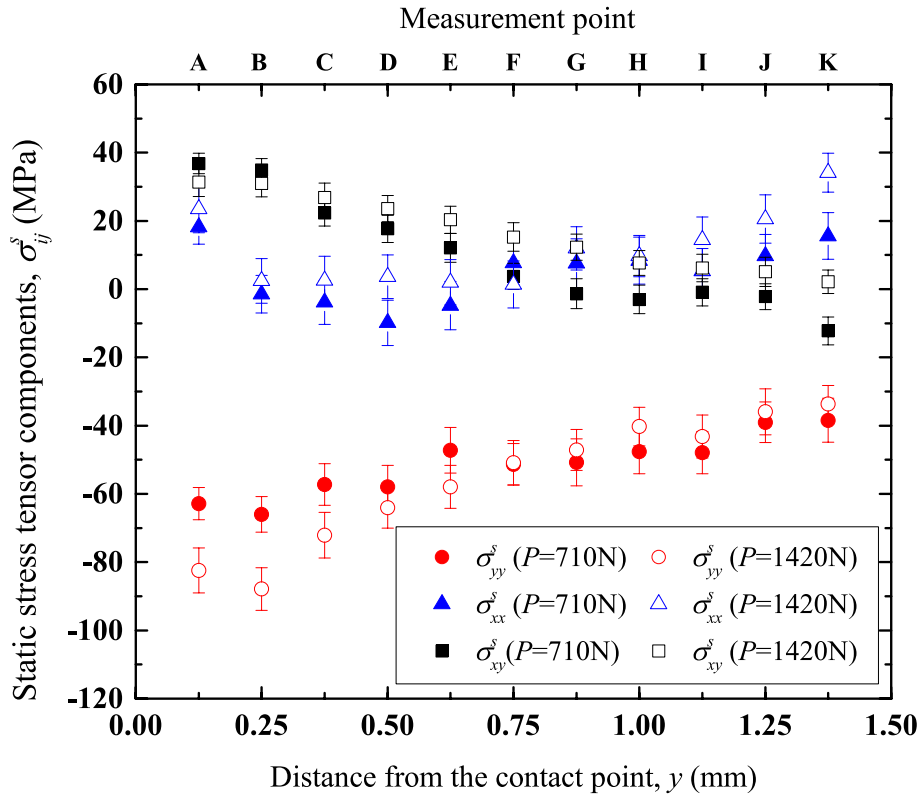
(a)
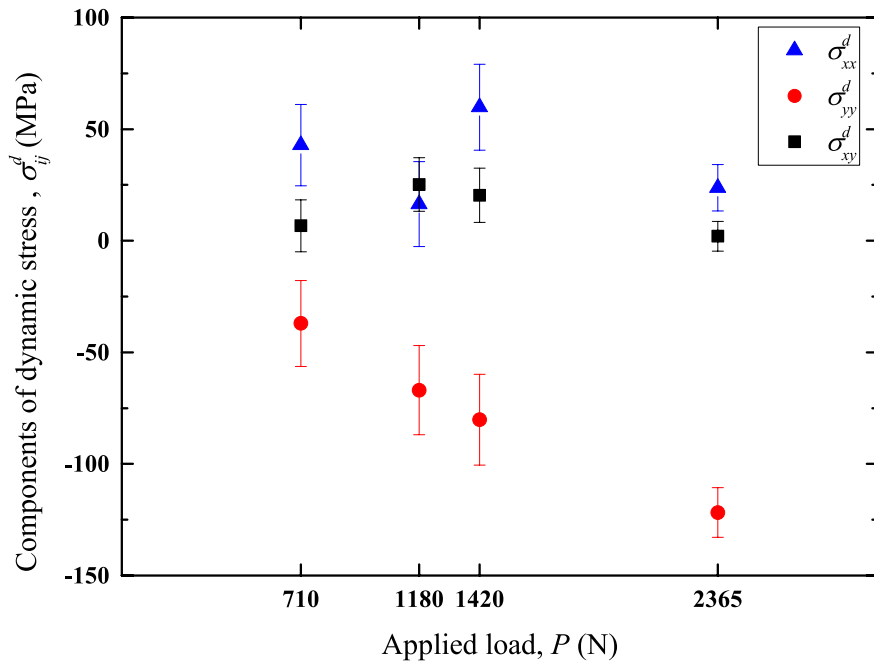


(b)

**Figure 4** – **Measured components of the stress tensor (a) in static case at 2 levels of loads at points**
***A - K* (b) in dynamic (stroboscopic) case at 4 levels of load at point *B* – see Figure 1a**
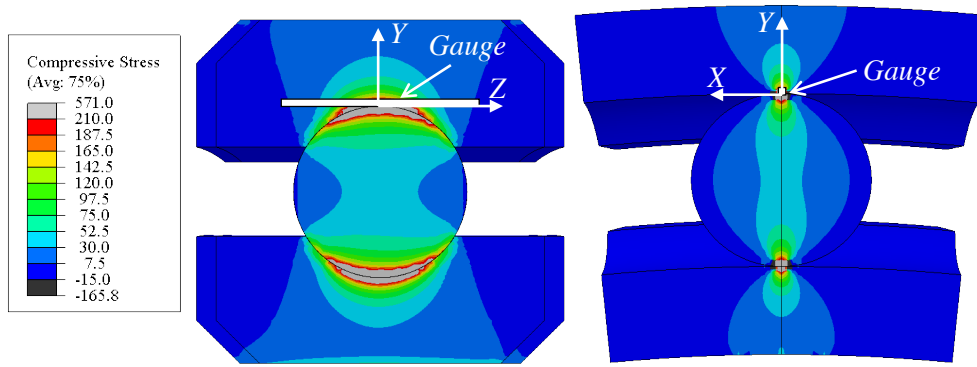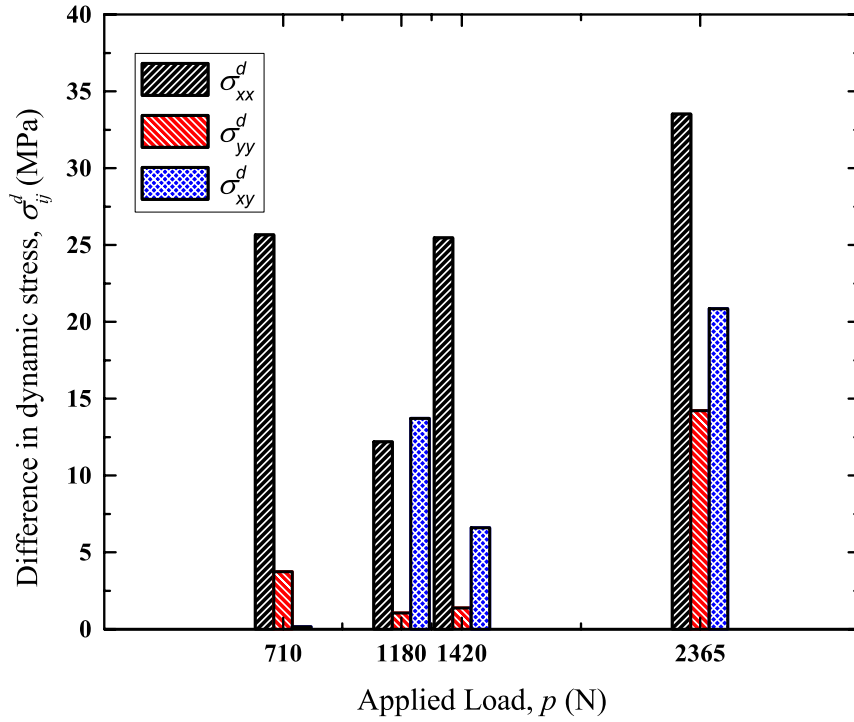
(a)
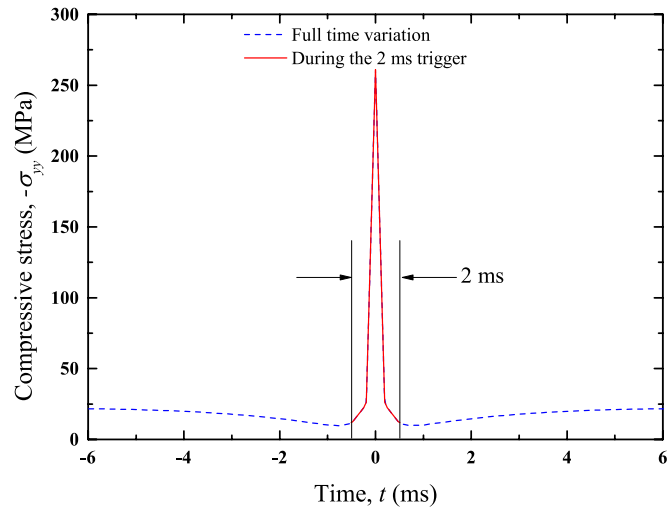


(b)
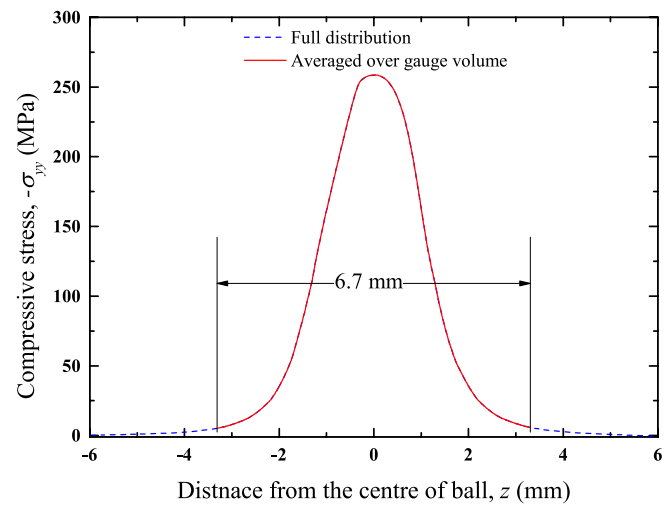


(c)

**Figure 5 – Finite element results at *p* = 1420 N (a) Stress field in XY and YZ planes in the middle of 2 ms triggering period - the gauge volume is plotted as a white box (b) the distribution of compressive stress at the point of contact as function of time (c) the distribution of compressive stress along the gauge volume in the middle of 2 ms triggering period**
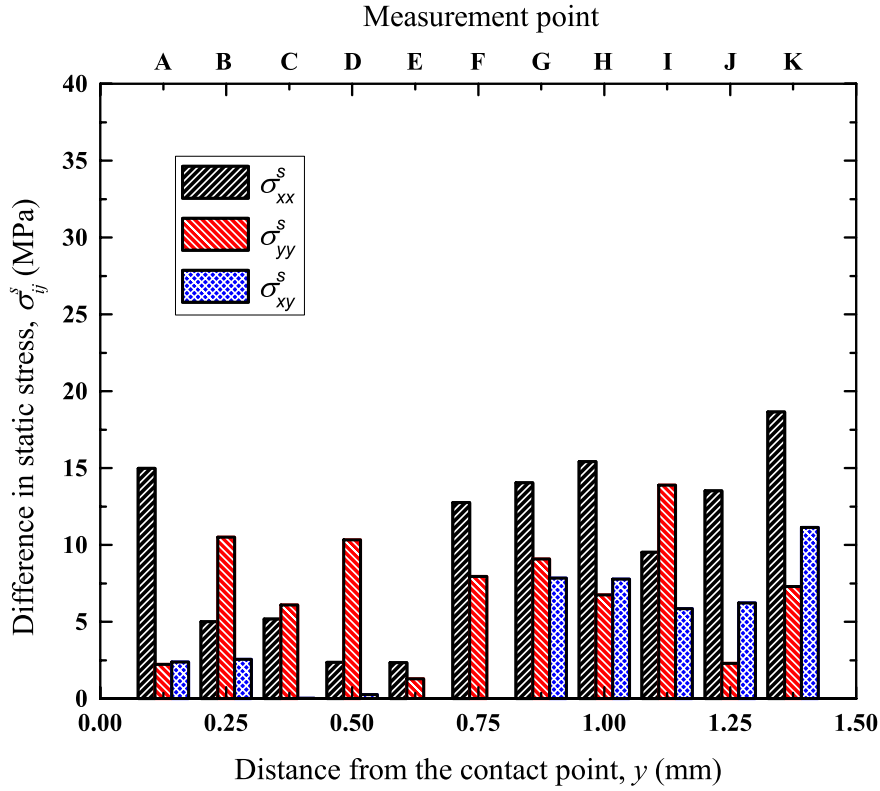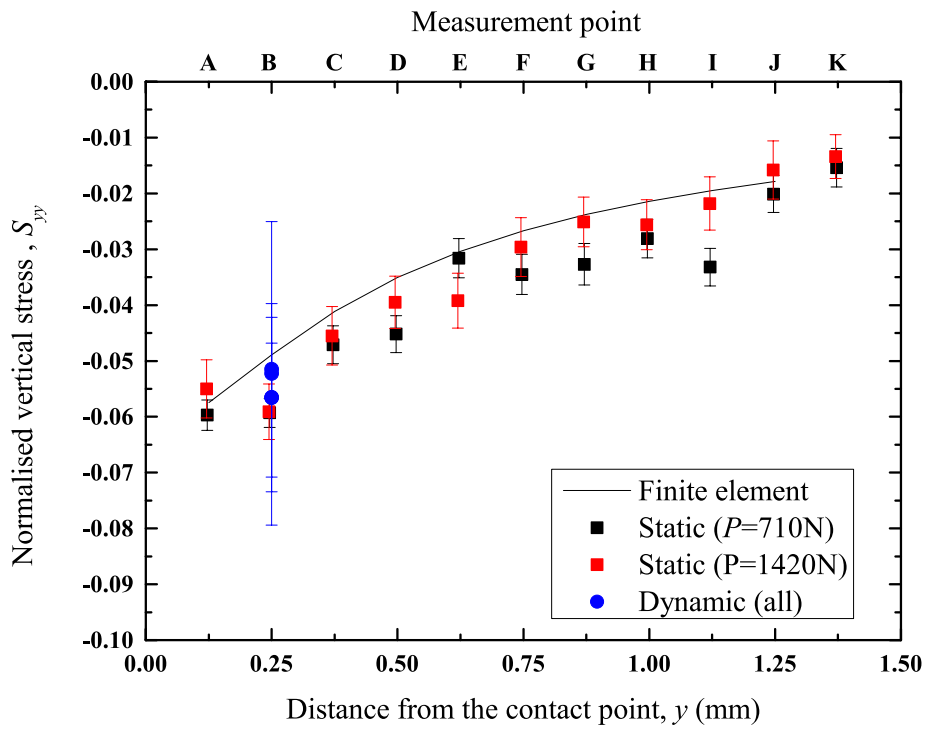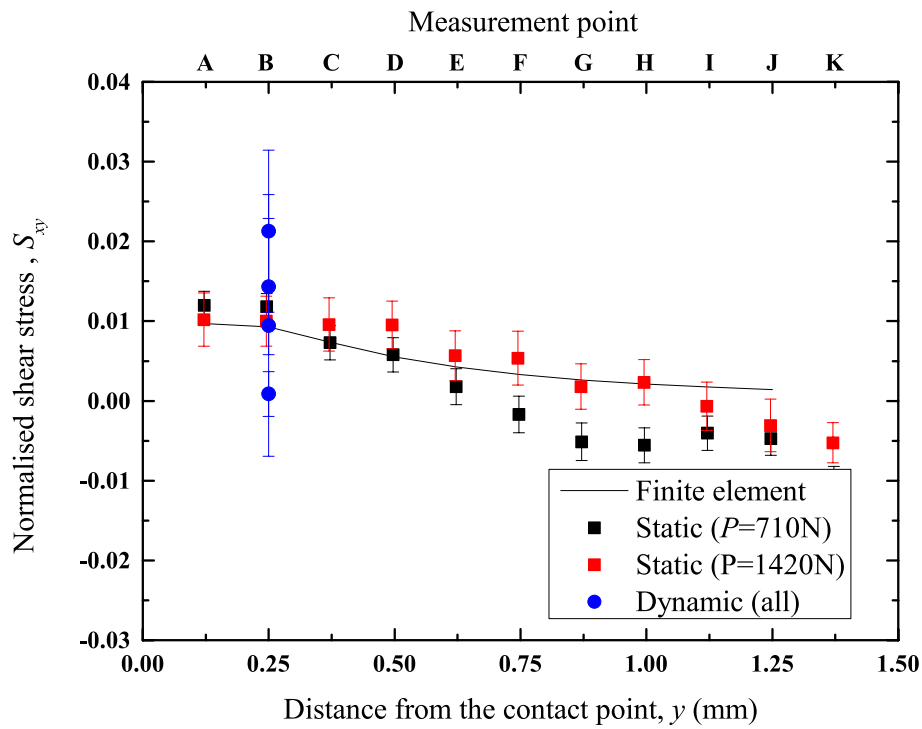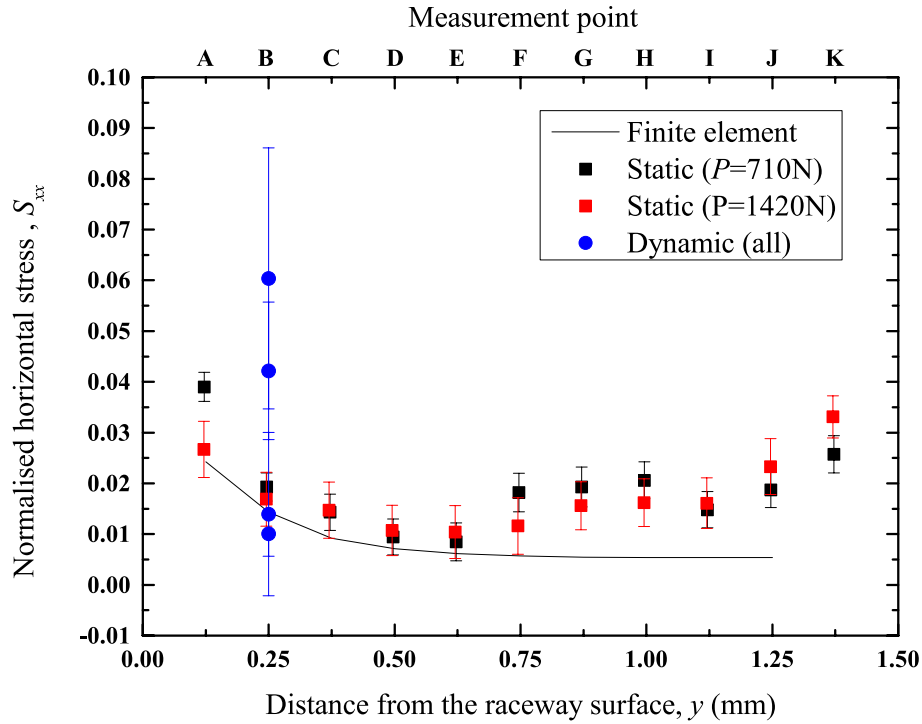
(a)
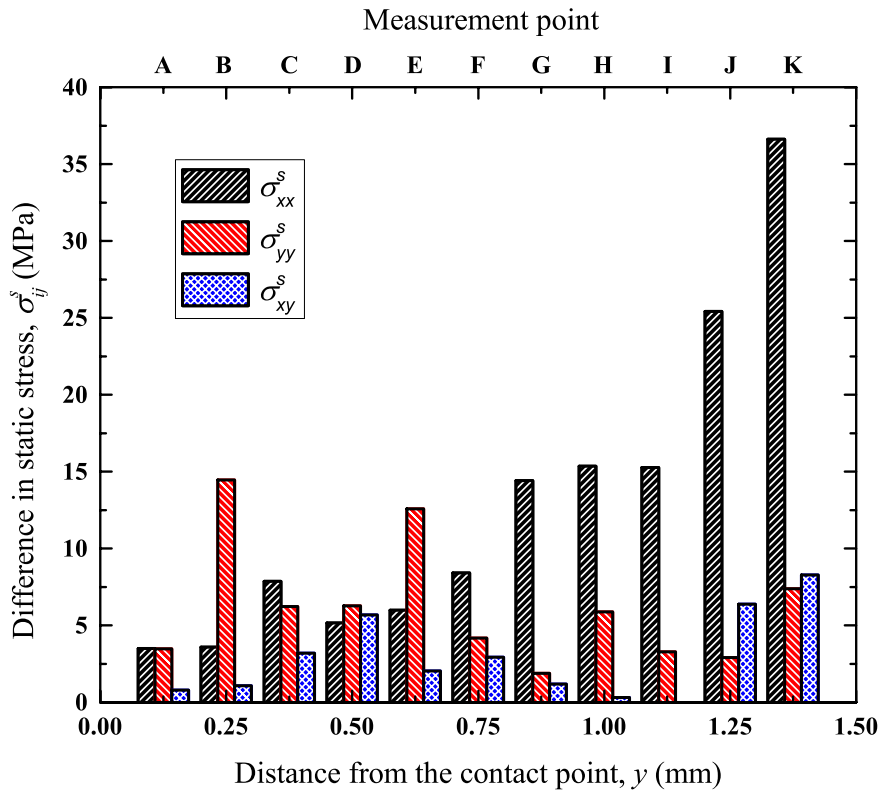


(b)

(c)

**Figure 6** – **Difference of stress tensor components between finite element simulation and experimental measurements (a) static at $p$ = 710 N at points $A$ - $K$ (b) static at $p$ = 1420 at points $A$ - $K$ (c) dynamic at point $B$ at various loads**

(a)



(b)

Figure 7 –Comparison of normalised stress tensor components for static, dynamic (stroboscopic) and finite element simulations (a) normalised normal stress in *X* direction $S_{xx}$ (b) normalised stress in *Y* direction $S_{yy}$ (c) normalised shear stress in *XY* direction $S_{xy}$